


Spin-wave dispersion of 3d ferromagnets based on quasiparticle self-consistent GW calculationsH. Okumura ^{*}*Division of Materials and Manufacturing Science, Graduate School of Engineering, Osaka University, Suita, Osaka 565-0871, Japan*

K. Sato

*Division of Materials and Manufacturing Science, Graduate School of Engineering, Osaka University, Suita, Osaka 565-0871, Japan
and Center for Spintronics Research Network (CSRN), Osaka University, Toyonaka, Osaka 560-8531, Japan*

T. Kotani

Department of Applied Mathematics and Physics, Tottori University, Tottori 680-8552, Japan

(Received 16 April 2019; published 14 August 2019)

We calculate transverse spin susceptibility in the linear response method based on the ground states determined in the quasiparticle self-consistent GW (QSGW) method. Then we extract spin-wave (SW) dispersions from the susceptibility. We treat bcc Fe, hcp Co, fcc Ni, and B2-type FeCo. Because of the better description of the independent-particle picture in QSGW, calculated spin stiffness constants for Fe, Co, and Ni give much better agreement with experiments in QSGW than those in the local density approximation (LDA); the stiffness for Ni in LDA is two times greater than in experiment. For Co, both acoustic and optical branches of SWs agree with experiment. As for FeCo, we have some discrepancy between the spin stiffness in QSGW and that in experiment. We may need further theoretical and experimental investigations on the discrepancy.

DOI: [10.1103/PhysRevB.100.054419](https://doi.org/10.1103/PhysRevB.100.054419)**I. INTRODUCTION**

Spin waves (SWs) are one of the important factors to control magnetic properties of material. SWs are excited at considerably lower temperatures than room temperature (RT), and their energy range typically lies within a few hundred meV. When one magnetic moment is tilted from the parallel spin configuration, the exchange interaction triggers the SW propagation throughout the material as collective excitation. We can observe SWs in bulk materials by inelastic neutron scattering experiments, e.g., in bcc Fe [1], fcc Ni [2], and even in half metals like perovskite $\text{La}_{0.7}\text{Sr}_{0.3}\text{MnO}_3$ [3]. In addition to collective excitation, another magnetic excitation like spin-flip excitation is called Stoner excitation, whose excitation energy is related to the exchange splitting ΔE_x . We can experimentally observe Stoner excitation by high-energy experiments such as spin-polarized electron energy loss spectroscopy (SPEELS) [4]. High-energy SWs are strongly damped because of the hybridization with the Stoner excitation.

Let us explain how we determine the spin stiffness D experimentally. From the macroscopic point of view, the Bloch $T^{\frac{3}{2}}$ rule [5] in the temperature dependence of magnetization $M(T)$ is derived from the SW theory. For the wave vector $\mathbf{q} \sim 0$, the SW dispersion $\omega(\mathbf{q})$ behaves as $\omega(\mathbf{q}) = D\mathbf{q}^2$. Since this behavior of $\omega(\mathbf{q})$ results in the $T^{\frac{3}{2}}$ rule in low temperature, we can determine D by analyzing the temperature dependence of magnetization [6].

We mainly have three methods to calculate $\omega(\mathbf{q})$ in the first-principles methods. The first one is the Lichtenstein formula (LF) [7]. Assuming the Heisenberg model, we calculate exchange interaction J_{ij} or its Fourier transform $J(\mathbf{q})$ based on the magnetic force theorem [8]. Here i, j are for site indices. Then $\omega(\mathbf{q})$ is calculated from $J(\mathbf{q})$. In Ref. [7], J_{ij} was calculated up to the second nearest neighbors, resulting in D , which are in good agreement with experiments for Fe and Ni. Later, Pajda *et al.* investigated the convergence of D for a range of neighbors and found that converged D are in good agreement with experiments for Fe but overestimated for Ni [9].

The second method is the frozen magnon method (FMM) [10], which assumes the Heisenberg model as in LF. In FMM, we employ the adiabatic approximation; namely, we neglect motions of the magnetic moment compared to electron motions. Then we calculate $J(\mathbf{q})$ from the constraint of spin-spiral configurations with the fixed magnitude of the magnetic moment. Once we get $J(\mathbf{q})$, we solve the eigenvalue problem for deriving $\omega(\mathbf{q})$. This method works well for bcc Fe [10,11]. Note that we cannot describe the decay of collective SWs (Stoner damping) in either of these two methods.

The third method is the linear response (LR) method for transverse spin susceptibility $R^{+-}(\mathbf{q}, \omega)$ [12]. The LR method directly gives $\omega(\mathbf{q})$ in the reciprocal space. Cooke *et al.* first introduced the LR method for calculating $R^{+-}(\mathbf{q}, \omega)$, and they discussed Stoner damping in SWs in bcc Fe and fcc Ni [13]. Savrasov treated spin fluctuations based on the many-body perturbation theory and reproduced the experimental $\omega(\mathbf{q})$ [14]. Karlsson and Aryasetiawan also calculated $R^{+-}(\mathbf{q}, \omega)$ based on the Green's function method [15]. From a view of computational efficiency, Şaşıoğlu *et al.* proposed

^{*}okumura.haruki@mat.eng.osaka-u.ac.jp

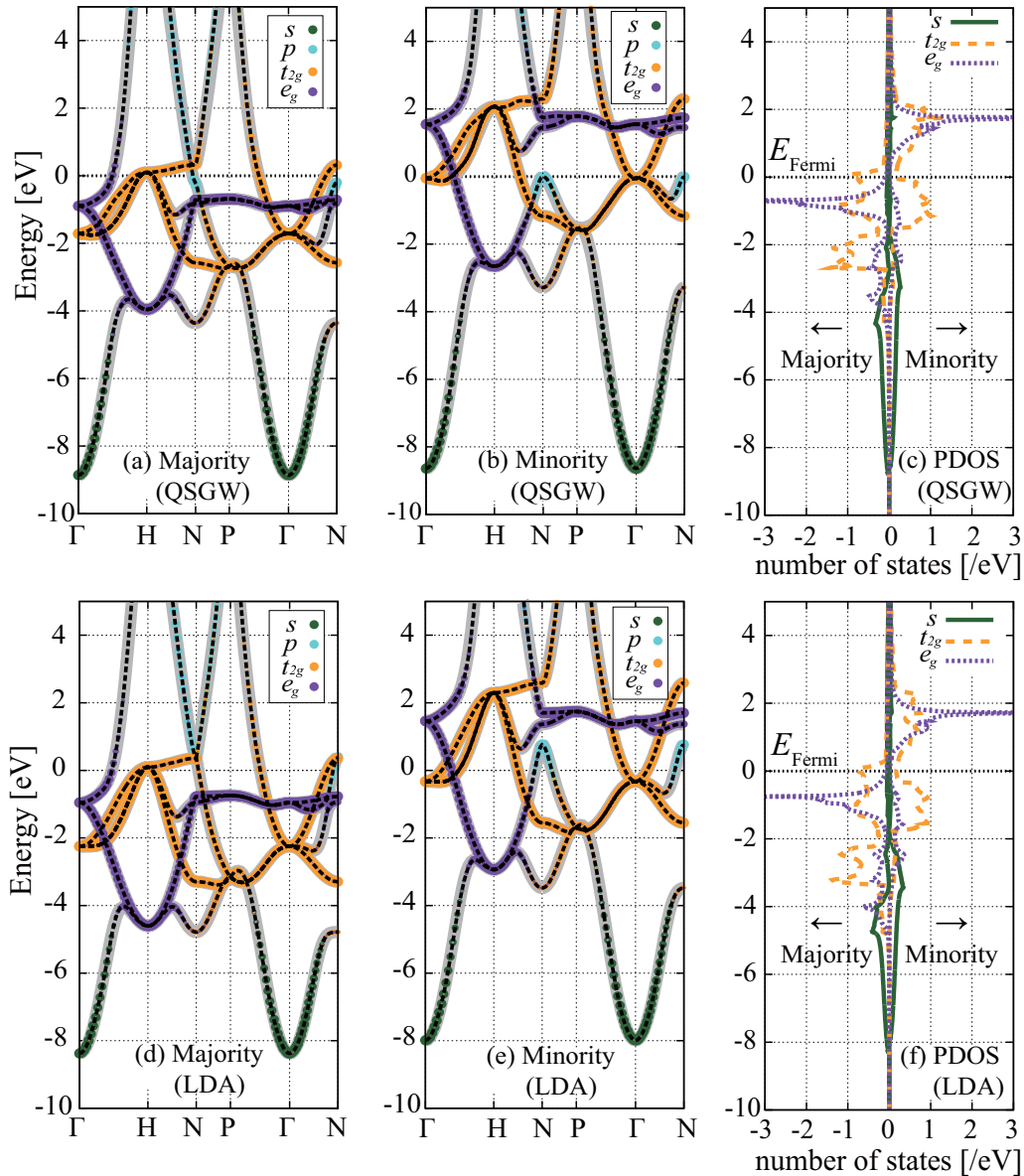


FIG. 1. Calculated band structures of Fe in QSGW [(a) majority spin, (b) minority spin] and in LDA [(d) majority spin, (e) minority spin]. The interpolated bands based on 9 MLWFs are also shown (broken line) with original bands (bold gray line). Size of colored circles on the bands shows the weight of MLWF bands. Partial density of states for $4s$, t_{2g} , and e_g in QSGW and LDA are shown in (c) and (f). Fermi energy E_{Fermi} is set to 0 eV.

a LR method with the maximally localized Wannier function (MLWF) [16]. In the method, we decrease to the second power of the number of a Wannier basis set and we can decrease the calculation cost. With this efficient method, we can use fine \mathbf{q} mesh for calculating $R^{+-}(\mathbf{q}, \omega)$.

These three methods mainly have been applied to the ground states given in the local density approximation (LDA). However, the ground state given in LDA is not necessarily good enough. For example, Sponza *et al.* show that $3d$ bandwidth and ΔE_x in LDA are not good enough to calculate $\omega(\mathbf{q})$ [17]. In antiferromagnetic transition metal oxides such as NiO and MnO, the calculated $\omega(\mathbf{q})$ does not agree with the experiment due to too small ΔE_x and too small band gap [18]. Serious disagreement is also found in the $\omega(\mathbf{q})$ in $\text{La}_{0.7}\text{Sr}_{0.3}\text{MnO}_3$, for which LDA fails to

reproduce the half-metallic electronic structure of that compound [19]. It is possible to start from the ground states of LDA + U ; however, we sometimes have difficulty in determination of U . This may suggest a limitation of LDA + U itself.

To overcome such limitations in LDA, Kotani *et al.* calculated $\omega(\mathbf{q})$ for strongly correlated materials in an LR method for the ground states determined in the quasiparticle self-consistent GW (QSGW) method [18, 19]. Then we see reasonable agreement with experiments for NiO and MnO because QSGW gives good descriptions of the band quantities such as ΔE_x and band gaps [20]. We expect such good agreement for a wide-range of materials. However, Kotani's LR method used in Refs. [18, 19] is too simple to apply to a wide range of materials.

TABLE I. t_{2g} level of Fe at Γ for the minority spin, and that at N for the majority spin. These are in LDA and QSGW, in addition to the experimental data by ARPES [34]. Energy is relative to E_{Fermi} .

	Band Energy (eV)		
	LDA	QSGW	Expt. [34]
Γ (minority)	-0.32	-0.11	-0.19
N (majority)	-0.74	-0.68	-0.57

Thus we implemented the efficient LR method to calculate $R^{+-}(\mathbf{q}, \omega)$ based on the MLWF given by Şaşıoğlu *et al.* [16] in the QSGW calculation package ECALJ compiled by Kotani *et al.* [21]. We demonstrate how the method works for typical ferromagnets such as bcc Fe, fcc Ni, hcp Co, and B2 FeCo (CsCl structure), and we discuss the difference between LDA and QSGW. Except for FeCo, the SWs in QSGW

agree with experiments. We find some discrepancies for FeCo.

II. COMPUTATIONAL METHODS

A. Quasiparticle self-consistent GW

Until now, varieties of GW calculations based on Hedin's GW approximation [22,23] have been performed since it was introduced in first-principles calculations by Hyberstein and Louie [24]. Most of the GW calculations are so-called one-shot GW. Starting from G^0 for the one-body Hamiltonian in LDA $\mathcal{H}_0^{\text{LDA}}$, we calculate corrections to the eigenvalues of $\mathcal{H}_0^{\text{LDA}}$ to reproduce quasiparticle energies. In the one-shot GW, the self-energy for the corrections is given as $\Sigma(1, 2) = iG^0(1, 2)W(1^+, 2)$, where we use the notation $1 \equiv (\mathbf{r}_1, t_1)$. The screened Coulomb interaction $W(1^+, 2)$ is calculated as $W = (1 - vP)^{-1}v$ from the bare Coulomb interaction v and the polarization function $P = -iG^0 \times G^0$. The one-shot GW

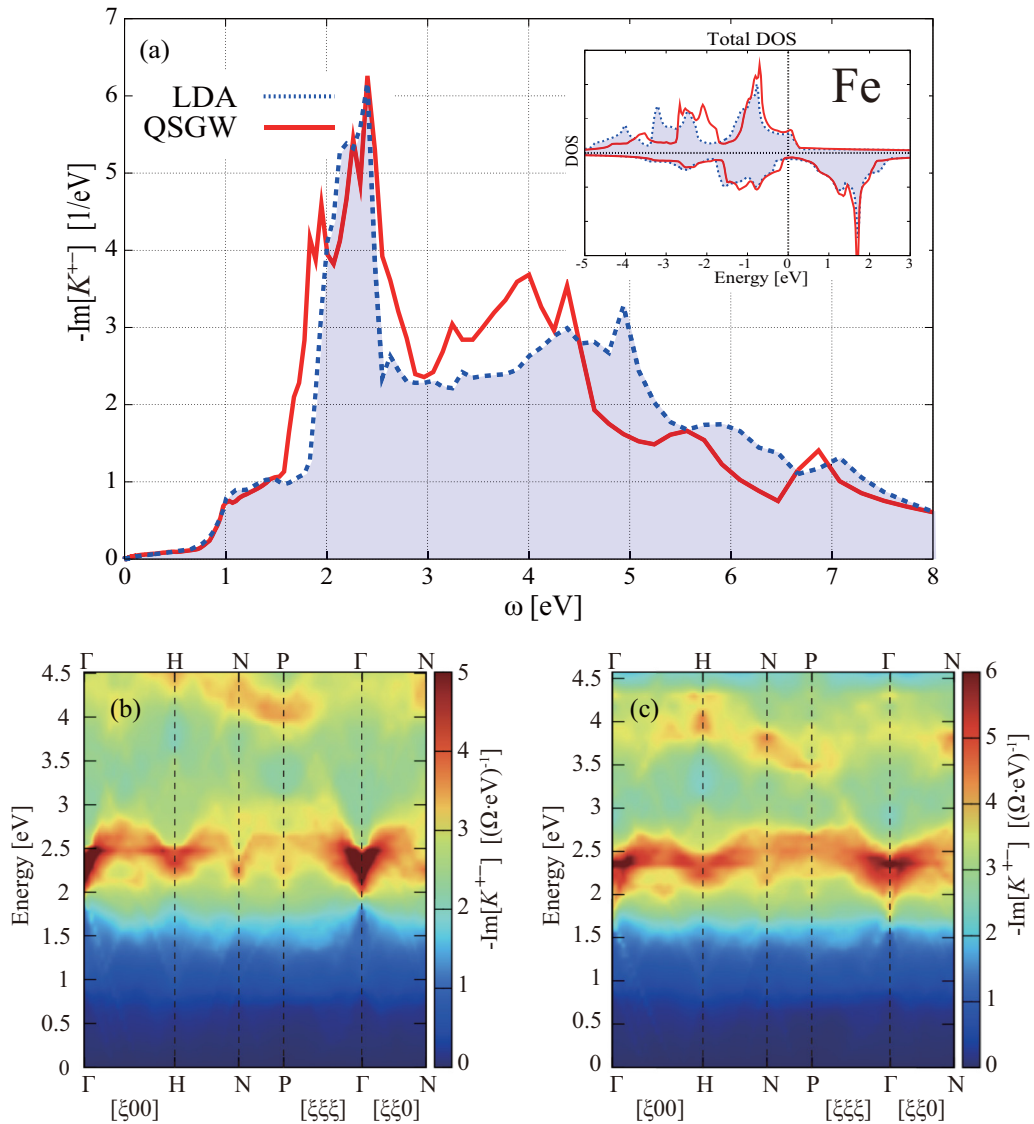


FIG. 2. (a) Calculated $-\text{Im}[K^{+-}(\mathbf{q} = 0, \omega)]$ in Fe in QSGW (red bold line) and in LDA (blue broken line). The inset is the total density of states in Fe. Panels (b) and (c) show calculated $-\text{Im}[K^{+-}(\mathbf{q}, \omega)]$ along the BZ symmetry line in LDA and QSGW, respectively. Ω is the unit cell volume.

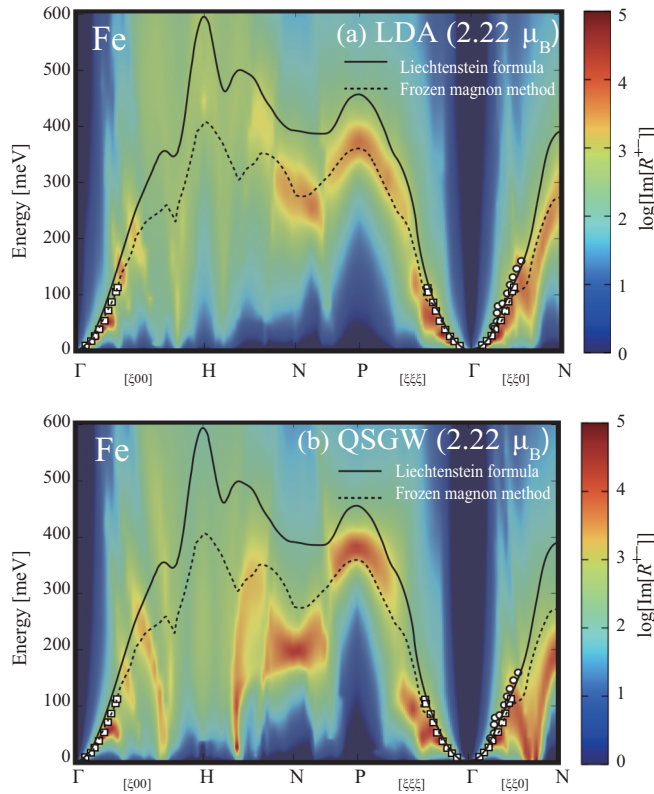


FIG. 3. $\text{Im}[R^{+-}(\mathbf{q}, \omega)]$ for Fe (a) in LDA and (b) in QSGW, showing the SW dispersion; we see slight discontinuities because of the mesh of used \mathbf{k} points. Results with LF [9] (solid line) and those with FMM [10] (broken line) are superposed. Experimental data by neutron scattering are indicated by open squares (Fe (12% Si) at RT [1]) and open circles (pure Fe at 10 K [36]).

has a shortcoming since the one-shot GW is just a perturbation on top of $\mathcal{H}_0^{\text{LDA}}$.

To overcome the shortcoming of the one-shot GW , we utilize the QSGW method [25–27] implemented in the ECALJ package [21]. Let us summarize the QSGW method. First, recall the above GW procedure which can be applicable to any static one-body Hamiltonian $\mathcal{H}_0(\mathbf{r}, \mathbf{r}')$ as

$$\mathcal{H}_0(\mathbf{r}, \mathbf{r}') = -\frac{\nabla^2}{2} + V_{\text{ext}} + V_{\text{H}} + V_{\text{xc}}(\mathbf{r}, \mathbf{r}'), \quad (1)$$

where we have the external potential V_{ext} , the Hartree potential V_{H} , and the nonlocal exchange-correlation potential $V_{\text{xc}}(\mathbf{r}, \mathbf{r}')$. With $\Sigma(1, 2) = iG^0(1, 2)W(1^+, 2)$, where $G^0 = 1/(\omega - \mathcal{H}_0)$, we have the energy-dependent one-body Hamiltonian $\mathcal{H}(\mathbf{r}, \mathbf{r}'; \omega)$ as

$$\mathcal{H}(\mathbf{r}, \mathbf{r}'; \omega) = -\frac{\nabla^2}{2} + V_{\text{ext}} + V_{\text{H}} + \Sigma(\mathbf{r}, \mathbf{r}'; \omega). \quad (2)$$

That is, the GW approximation gives a procedure $\mathcal{H}_0 \rightarrow \mathcal{H}$. QSGW requires “quasiparticle self-consistency,” that is, minimization of the difference between \mathcal{H}_0 and \mathcal{H} . The minimization gives the procedure $\mathcal{H} \rightarrow \mathcal{H}_0$, replacing the ω -dependent Σ in Eq. (2) with the static nonlocal exchange-correlation

potential V^{xc} as

$$V^{\text{xc}} = \frac{1}{2} \sum_{ij} |\psi_i\rangle \{ \text{Re}[\Sigma(\varepsilon_i)]_{ij} + \text{Re}[\Sigma(\varepsilon_j)]_{ij} \} \langle \psi_j|, \quad (3)$$

where eigenvalues ε_i and eigenfunctions ψ_i are those of \mathcal{H}_0 . This defines a procedure to give a new \mathcal{H}_0 , $\mathcal{H} \rightarrow \mathcal{H}_0$. Thus we finally have a “quasiparticle self-consistency” cycle $\mathcal{H}_0 \rightarrow \mathcal{H} \rightarrow \mathcal{H}_0 \rightarrow \mathcal{H} \rightarrow \dots$ (or $G^0 \rightarrow G \rightarrow G^0 \rightarrow \dots$) until converged.

B. Dynamical magnetic susceptibility

In LR, we follow the procedure given in Refs. [16,28]. Here we treat the transverse spin susceptibility $R^{+-}(1, 2)$, which describes the response of the expectation value of a spin density operator $\hat{\sigma}^+(1)$ to the external magnetic field $B^-(2)$ as

$$R^{+-}(1, 2) = \frac{\delta \langle \hat{\sigma}^+(1) \rangle}{\delta B^+(2)}, \quad (4)$$

where $1 = (\mathbf{r}_1, t_1)$. See Eq. (20) in Ref. [28]. Here the expectation value of $\hat{\sigma}^+(1)$ is given as

$$\langle \hat{\sigma}^+(1) \rangle = -i \sum_{\alpha, \beta} \sigma_{\beta\alpha}^+ G_{\alpha\beta}(1, 1^+) \quad (\alpha, \beta \in \{\uparrow, \downarrow\}), \quad (5)$$

where $G(1, 1^+)$ is the single-particle Green’s function from 1 to 1^+ . For our calculation below, it is convenient to consider the four-point representation $R_{\uparrow\downarrow}^{(4)}(12, 34)$. The trace of matrix $R_{\uparrow\downarrow}^{(4)}(11, 33)$ leads to the two-point representation $R^{+-}(1, 2)$.

In order to obtain $R_{\uparrow\downarrow}^{(4)}(12, 34)$, we solve the Bethe-Salpeter equation where we use the static screened Coulomb interaction $W(1^+, 2)$ which is $\propto \delta(t_1 - t_2)$. It is

$$R_{\uparrow\downarrow}^{(4)}(12, 34) = K_{\uparrow\downarrow}(12, 34) + \int \int K_{\uparrow\downarrow}(12, 56) \times W(5^+, 6) R_{\uparrow\downarrow}(56, 34) d5d6, \quad (6)$$

where $K_{\uparrow\downarrow}(12, 34)$ is the noninteracting two-particle (particle-hole with opposite spin) propagator given as

$$-K_{\uparrow\downarrow}(12, 34) = -iG_{\uparrow}^0(1, 3)G_{\downarrow}^0(4, 2^+), \quad (7)$$

where we consider $t_1 = t_2$ and $t_3 = t_4$, i.e., $K_{\uparrow\downarrow}(\mathbf{r}_1, \mathbf{r}_2; \mathbf{r}_3, \mathbf{r}_4; t_1 - t_3)$. The Fourier transform is from $t_1 - t_3$ to ω . We symbolically solve Eq. (6) to be $R = K + KWK + KWKWK + \dots = K(1 - WK)^{-1}$, where the numerator K describes the Stoner excitations, whereas zeros of the denominator $(1 - WK)$ give the collective excitation.

This $K_{\uparrow\downarrow}$ is given as

$$\begin{aligned} -K_{\uparrow\downarrow}(\mathbf{r}_1, \mathbf{r}_2; \mathbf{r}_3, \mathbf{r}_4; \omega) &= \sum_{\mathbf{k}, n}^{\text{occ}} \sum_{\mathbf{k}', n'}^{\text{unocc}} \frac{\Psi_{\mathbf{k}n\downarrow}^*(\mathbf{r}_2) \Psi_{\mathbf{k}n\downarrow}(\mathbf{r}_4) \Psi_{\mathbf{k}'n'\uparrow}(\mathbf{r}_1) \Psi_{\mathbf{k}'n'\uparrow}^*(\mathbf{r}_3)}{\omega - (\varepsilon_{\mathbf{k}'n'\uparrow} - \varepsilon_{\mathbf{k}n\downarrow}) + i\delta} \\ &+ \sum_{\mathbf{k}, n}^{\text{unocc}} \sum_{\mathbf{k}', n'}^{\text{occ}} \frac{\Psi_{\mathbf{k}n\downarrow}^*(\mathbf{r}_2) \Psi_{\mathbf{k}n\downarrow}(\mathbf{r}_4) \Psi_{\mathbf{k}'n'\uparrow}(\mathbf{r}_1) \Psi_{\mathbf{k}'n'\uparrow}^*(\mathbf{r}_3)}{-\omega - (\varepsilon_{\mathbf{k}n\downarrow} - \varepsilon_{\mathbf{k}'n'\uparrow}) + i\delta}, \end{aligned} \quad (8)$$

where \mathbf{k}, \mathbf{k}' are in the first Brillouin zone, $n(n')$ is the band index summed over occupied (unoccupied) states, $\varepsilon_{\mathbf{k}n\uparrow}$ ($\varepsilon_{\mathbf{k}n\downarrow}$)

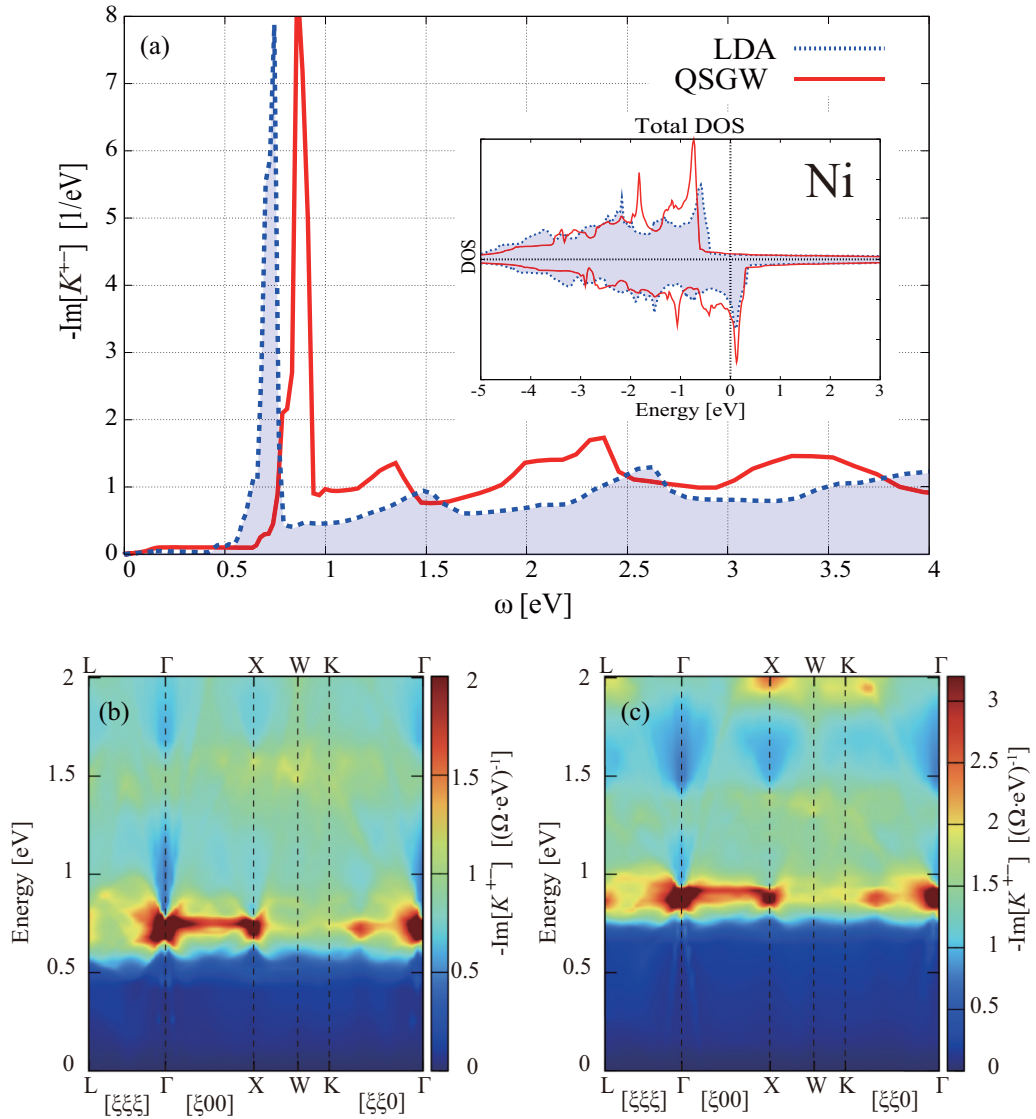


FIG. 4. (a) $-\text{Im}[K^{++}(\mathbf{q} = 0, \omega)]$ in Ni in QSGW (red bold line) and in LDA (blue broken line). The inset is the total density of states in Ni. Panels (b) and (c) calculate $-\text{Im}[K^{++}(\mathbf{q}, \omega)]$ along the BZ symmetry line in LDA and QSGW, respectively. Ω is the unit cell volume.

is the n th majority (minority) band energy at \mathbf{k} , and Ψ is the eigenfunction of \mathcal{H}_0 .

As mentioned in Ref. [16], in order to satisfy the Goldstone theorem $\omega(\mathbf{q}) \rightarrow 0$ ($\mathbf{q} \rightarrow 0$), we need to introduce a factor η for $R = K(1 - \eta WK)^{-1}$. In principle, the Goldstone theorem should be automatically satisfied with the LR method since we expect that the LR method evaluates the second derivative of the total energy of the ground states. However, our LR is not formulated to reproduce the second derivative exactly; furthermore, QSGW is not formulated to minimize the total energy. This simple scaling by introducing η is a quick remedy to satisfy the theorem; its deviations from unity show the size of vertex corrections, which should be added to the interaction W . The calculated η of LDA (QSGW) are 1.15 (1.19), 1.41 (1.87), 1.26 (1.33), and 1.05 (0.87) for Fe, Ni, Co, and FeCo, respectively. These η are in good agreement with previous calculations 1.28, 1.5, and 1.33 for Fe [28], Ni [16], and FeCo [28]. The deviations are not small enough. We may need to treat the vertex correction accurately in order

to override the ambiguity due to this quick remedy in the future.

C. Wannier representation

Based on Refs. [29,30], we generate MLWFs from eigenfunctions of LDA or QSGW. Once we generate MLWFs, we can obtain the Wannier representation of $R^{\uparrow\downarrow}$ as follows.

In the Wannier basis, we expand eigenfunctions as

$$\Psi_{\mathbf{k}n}(\mathbf{r}) = \sum_{\mathbf{R}'} a_{\mathbf{R}'}^{\mathbf{k}n} w_{\mathbf{R}'}^{\mathbf{k}}(\mathbf{r}), \quad (9)$$

where $a_{\mathbf{R}'}^{\mathbf{k}n}$ is the expansion coefficient, \mathbf{R} is atomic position in a primitive cell, and i is the Wannier orbital (e.g., $i = 3d_{xy}$) of each atom on \mathbf{R} . $w_{\mathbf{R}'}^{\mathbf{k}}(\mathbf{r})$ is represented as a complete set of orthogonal basis $\{w_{\mathbf{R}'}(\mathbf{r})\}$,

$$w_{\mathbf{R}'}^{\mathbf{k}}(\mathbf{r}) = \frac{1}{\sqrt{N}} \sum_{\mathbf{T}} w_{\mathbf{R}'}(\mathbf{r} - \mathbf{R} - \mathbf{T}) \exp(i\mathbf{k} \cdot \mathbf{T}), \quad (10)$$

TABLE II. Calculated stiffness constant D for Fe, Ni, Co, and FeCo. The results by other groups are shown together: the LR [28], with the LF [9], and with the time-dependent DFT (TDDFT) [37] (on average). In addition we show inelastic neutron scattering data [1,2,6,40,44,44,46].

Material	D (meV \AA^2)					
	LR (LDA)	LR (QSGW)	Expt.	LR (GGA) [28]	LF [9]	TDDFT [37]
bcc Fe	155	222	230 (RT) [1] 280 (4.2 K) [6]	248	250	189
fcc Ni	873	449	433 [2] 555 [40]		756	1097
hcp Co [100]	565	486	478 [43]			
hcp Co [001]	752	532	410 [43] 510 [44]			
B2 FeCo	407	307	450–500 [46]			

where \mathbf{T} is the lattice translation vector and N is the normalization constant satisfying the Born–von Karman boundary condition. By using the orthogonality, the eigenvalue equations $\mathcal{H}\Psi_{\mathbf{k}n}(\mathbf{r}) = \varepsilon_{\mathbf{k}n}\Psi_{\mathbf{k}n}(\mathbf{r})$ can be rewritten with this Wannier representation,

$$\sum_{\mathbf{R}'j} H_{\mathbf{R}i\mathbf{R}'j}^{\mathbf{k}} a_{\mathbf{R}'j}^{\mathbf{k}n} = \varepsilon_{\mathbf{k}n} a_{\mathbf{R}i}^{\mathbf{k}n}, \quad (11)$$

where the Hamiltonian matrix with Wannier basis $H_{\mathbf{R}i\mathbf{R}'j}^{\mathbf{k}}$ is the Fourier transform of $H_{\mathbf{R}i\mathbf{R}'j}^{\mathbf{T}-\mathbf{T}'} \equiv \langle w_{\mathbf{R}i}(\mathbf{r} - \mathbf{R} - \mathbf{T}) | \mathcal{H} | w_{\mathbf{R}'j}(\mathbf{r} - \mathbf{R}' - \mathbf{T}') \rangle$.

Substituting Eqs. (9) and (10) into Eq. (8) and using the Fourier transform of real space, we will obtain the

time-ordered linear response function for a noninteracting system represented in a restricted Hilbert space,

$$\begin{aligned} & -K_{\mathbf{R}ij,\mathbf{R}'kl}^{\uparrow\downarrow}(\mathbf{q}, \omega) \\ &= \frac{1}{N} \sum_{\mathbf{k}} \sum_n^{\text{occ}} \sum_{n'}^{\text{unocc}} \frac{a_{\mathbf{R}j\beta}^{\mathbf{k}n*} a_{\mathbf{R}'l\beta}^{\mathbf{k}n} a_{\mathbf{R}i\alpha}^{\mathbf{k}+q\mathbf{n}'} a_{\mathbf{R}'k\alpha}^{\mathbf{k}+q\mathbf{n}'*}}{\omega - (\varepsilon_{\mathbf{q}+\mathbf{k}n'\uparrow} - \varepsilon_{\mathbf{k}n\downarrow}) + i\delta} \\ &+ \frac{1}{N} \sum_{\mathbf{k}} \sum_n^{\text{unocc}} \sum_{n'}^{\text{occ}} \frac{a_{\mathbf{R}j\beta}^{\mathbf{k}n*} a_{\mathbf{R}'l\beta}^{\mathbf{k}n} a_{\mathbf{R}i\alpha}^{\mathbf{k}+q\mathbf{n}'} a_{\mathbf{R}'k\alpha}^{\mathbf{k}+q\mathbf{n}'*}}{-\omega - (\varepsilon_{\mathbf{k}n\downarrow} - \varepsilon_{\mathbf{q}+\mathbf{k}n'\uparrow}) + i\delta}. \quad (12) \end{aligned}$$

We calculate the imaginary part of $-K_{\mathbf{R}ij,\mathbf{R}'kl}^{\uparrow\downarrow}(\mathbf{q}, \omega)$ by a tetrahedron method and obtain its real part by the Hilbert transform. The matrix element of $R_{\mathbf{R}ij,\mathbf{R}'kl}^{\uparrow\downarrow}$ is calculated through $R = K(1 - \eta WK)^{-1}$, where W is calculated in the random phase approximation (RPA) in the product basis technique developed in Ref. [31].

D. Calculation details

All of the calculation procedures above are implemented in the first-principles package ECALJ [20,21]. The ECALJ package is based on the linearized augmented plane wave and muffin-tin orbital (MTO) method (PMT method), which combines augmented plane wave (APW) and MTO basis sets. We also generate MLWFs in ECALJ. We perform LDA and QSGW calculations for band structures with $20 \times 20 \times 20$ and $16 \times 16 \times 16$ k -point meshes, respectively. We consider 9 MLWFs (spd) for the $3d$ elemental materials (Fe and Ni) and 18 MLWFs for hcp Co and binary FeCo. In the calculations of $K^{\uparrow\downarrow}$, we use a $48 \times 48 \times 48$ q -point mesh for the $3d$ elemental material and $24 \times 24 \times 24$ for binary FeCo. We use static and on-site W ; i.e., we take $W_{ijkl}(\omega) = W_{\mathbf{R}ij,\mathbf{R}kl}(\omega = 0)$. We use experimental lattice parameters $a = 2.867 \text{ \AA}$, $a = 3.524 \text{ \AA}$, and $a = 2.850 \text{ \AA}$ for Fe, Ni, and FeCo, respectively. For hcp Co, we use $a = 2.507 \text{ \AA}$ and $c = 4.070 \text{ \AA}$.

III. RESULTS AND DISCUSSION

A. bcc Fe

Figures 1(a)–1(c) show the majority and minority band structures and the partial density of states in QSGW for Fe, while Figs. 1(d)–1(f) in LDA as well. Calculated total magnetic moments in LDA and QSGW are both $2.22 \mu_B$ for Fe, in agreement with the experimental value $2.22 \mu_B$ [32], in

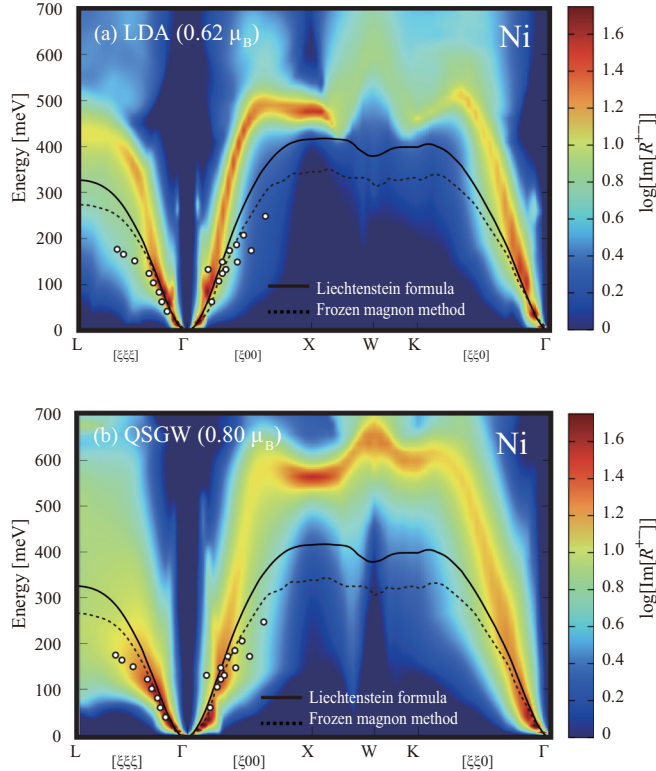


FIG. 5. $\text{Im}[R^{\pm}(\mathbf{q}, \omega)]$ for Ni in LDA (a) and in QSGW (b), showing the SW dispersion. We superpose other results with the LF [9] (solid line) and with FMM [10] (broken line). Experimental results by neutron scattering [41] are indicated by circles.

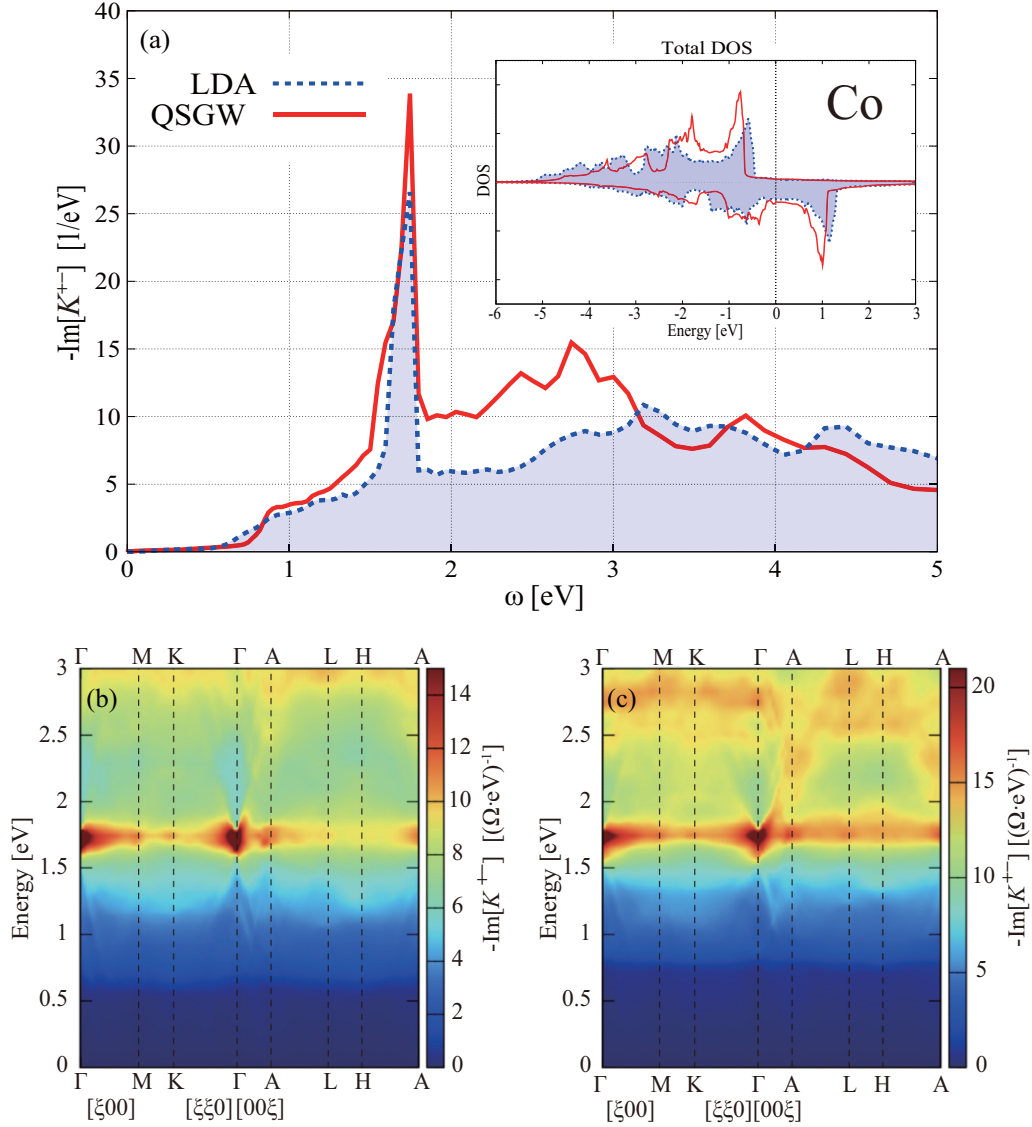


FIG. 6. (a) $-\text{Im}[K^{+-}(\mathbf{q} = 0, \omega)]$ in Co in QSGW (red bold line) and in LDA (blue broken line). The inset is total density of states in Co. Panels (b) and (c) show calculated $-\text{Im}[K^{+-}(\mathbf{q}, \omega)]$ along the BZ symmetry line in LDA and QSGW, respectively. Ω is the unit cell volume.

contrast to $2.93 \mu_B$ in the fully self-consistent GW method [33]. Our results are consistent with Ref. [17] by Sponza *et al.* The superposed Wannier band structures in Eq. (11) by broken lines are entirely on the original band structures by bold gray lines. The size of the colored circles shows the weights of each MLWF. In Table I, we show the t_{2g} of the minority spin at Γ and that of the majority spin at N in LDA and QSGW. QSGW gives better agreement with the angle-resolved photoemission spectroscopy (ARPES) data [34]. The 3d bandwidth in QSGW is a little smaller than that in LDA. Except for this difference, the overall shapes of the majority and the minority bands are similar in both LDA and QSGW.

Figure 2(a) shows $-\text{Im}[K^{+-}(\mathbf{q} = 0, \omega)]$ in LDA and in QSGW, where $K^{+-}(\mathbf{q}, \omega)$ means the trace of the matrix $K^{\uparrow\downarrow}$ given as $K^{+-}(\mathbf{q}, \omega) = \sum_{\mathbf{R}, i, j} K_{\mathbf{R}ii, \mathbf{R}jj}^{\uparrow\downarrow}(\mathbf{q}, \omega)$. We use a slightly different definition from Refs. [16, 28, 35]; thus it is not meaningful to compare absolute value of $K^{+-}(\mathbf{q}, \omega)$ with their results. As shown in the figure, QSGW gives smaller ΔE_x and 3d bandwidth, which is consistent with results by

Sponza *et al.* Roughly speaking, the shape of $-\text{Im}[K^{+-}(\mathbf{q} = 0, \omega)]$ agrees with the shape of the density of states (DOS) of the majority spin. The peak around 2 eV originates from the $t_{2g}^{\uparrow} - t_{2g}^{\downarrow}$ and $e_g^{\uparrow} - e_g^{\downarrow}$ transitions, i.e., vertical transitions to the unoccupied minority states above the Fermi energy E_{Fermi} from the occupied majority states just below the E_{Fermi} in Fig. 1. The second peak around 4 eV stems from another $e_g^{\uparrow} - e_g^{\downarrow}$ transition to $E_{\text{Fermi}} + 2$ eV in minority states from $E_{\text{Fermi}} - 2$ eV in majority states.

We see two features in the difference between LDA and QSGW in $-\text{Im}[K^{+-}(\mathbf{q} = 0, \omega)]$ shown in Fig. 2(a). One is that the width of the peak around 2 eV in QSGW is wider than that in LDA. The difference of DOS in LDA and QSGW cannot explain this fact; it can be due to the difference of eigenfunctions. The peak becomes wider in QSGW, probably because of the general tendency of QSGW that it makes a more significant difference between occupied 3d states and unoccupied 3d states. The former is more localized, and the latter more extended in comparison with the case in LDA. The

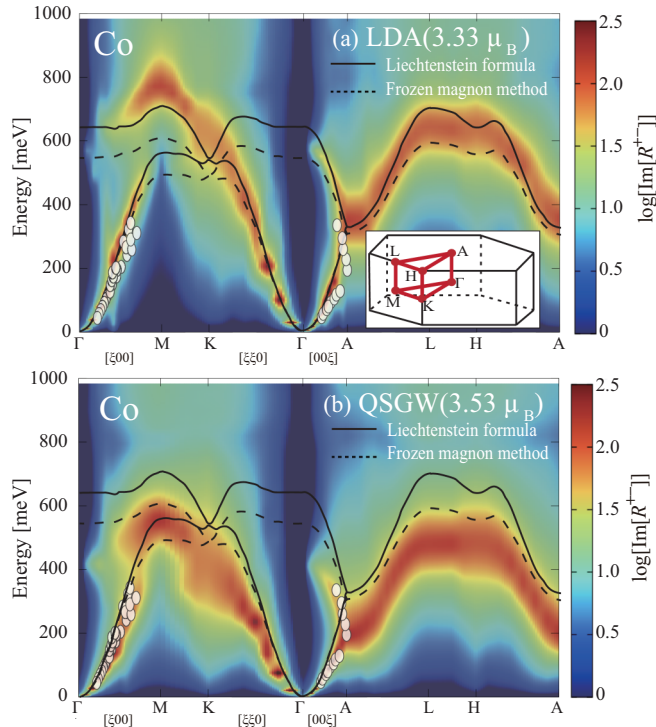


FIG. 7. $\text{Im}[R^{+-}(\mathbf{q}, \omega)]$ for Co in LDA (a) and in QSGW (b), showing the SW dispersion. The LF [9] (bold line) and the FMM calculation [10] (broken line) are also shown. Experimental data by neutron scattering [43] are indicated by circles. The inset shows the BZ for hcp Co and its symmetry lines.

other is the width due to the $3d$ band; corresponding to the width of the $3d$ band shown in the inset of Fig. 2(a), we see a narrower width in $-\text{Im}[K^{+-}(\mathbf{q} = 0, \omega)]$ in QSGW.

Figures 2(b) and 2(c) show the Stoner excitation spectrum $-\text{Im}[K^{+-}(\mathbf{q}, \omega)]$ in LDA and QSGW. Our LDA results give good agreement with Fig. 6 in Ref. [35]. We see red triangle-like strong intensity around Γ , especially in LDA. The center of the peak moves up as a function of \mathbf{q} . This is because the shifted q from Γ requires a corresponding energy shift to trace the peak of $-\text{Im}[K^{+-}(\mathbf{q}, \omega)]$ as a function of ω . This is explained in Fig. 7 of Ref. [35].

Figure 3 shows $\text{Im}[R^{+-}(\mathbf{q}, \omega)]$ in LDA (a) and in QSGW (b), where $R^{+-}(\mathbf{q}, \omega)$ means the trace of the matrix $R^{\uparrow\downarrow}$ given as $R^{+-}(\mathbf{q}, \omega) = \sum_{\mathbf{R}, i, j} R_{\mathbf{R}i, \mathbf{R}j}^{\uparrow\downarrow}(\mathbf{q}, \omega)$. We superpose experimental data [1,36] on it. We also superpose the SW dispersion calculated with the LF [9] in LDA, and that with FMM in LDA [10]. These are not only in (a) but also in (b) as a guide to the eye. As shown in Fig. 3, the peak broadening due to the Stoner damping can be seen even below 100 meV because bcc Fe is a weak ferromagnet, whose majority and minority $3d$ have relatively large DOS at E_{Fermi} as shown in the inset of Fig. 2(a). This results in relatively large low-energy Stoner excitations. It means that SWs are getting to be hybridized well with Stoner excitation immediately after departing from Γ . The strong damping around H is also seen in the previous calculation combining the generalized gradient approximation (GGA) and the MLWF approach with 6 MLWFs (*sd*) [28]. Our LDA calculation indicates Kohn

anomalies in Γ - H , H - N , and Γ - N , which are also found in the other calculations [9–11]. We checked calculations with a denser q -point mesh ($60 \times 60 \times 60$) and confirmed the strong anomaly at $2/3$ along Γ - N in LDA, and especially in QSGW. Reference [35] explains how such anomalies can be traced back to the band structures, although it does not give an explicit analysis. Real metals such as Fe can have complicated band structures, resulting in too complicated Fermi-surface-nesting-like phenomena to be analyzed. Thus, we also have not yet done such an analysis. We are somewhat skeptical as to whether it is worthwhile to do it or not.

In Table II, we summarize the calculated results of the stiffness constant D , with another LR result based on the GGA [28], and with that of the time-dependent density functional theory (TDDFT) [37]. To obtain D , we fit the calculated SW dispersion by quadratic functions. For the fitting, we just take peaks for small q as $|\mathbf{q}| < 0.20(\frac{2\pi}{a})$ where little Stoner damping occurs. Details for Fe and Ni are in the Supplemental Material [38]. LDA gives $D = 155 \text{ meV } \text{\AA}^2$, which is a little smaller than experiments $D = 230, 280 \text{ meV } \text{\AA}^2$ [1,6]. On the other hand, QSGW gives $D = 222 \text{ meV } \text{\AA}^2$ in much better agreement with the experimental values. Note that we see a contradiction between our LR (LDA) and the other two previous calculations, the LR (GGA) and the LF. Our value $D = 155 \text{ meV } \text{\AA}^2$ is too low in comparison with the other data 248, 250 $\text{meV } \text{\AA}^2$, although there is a smaller difference from $D = 189 \text{ meV } \text{\AA}^2$ in TDDFT. However, we currently have no definite idea to resolve the discrepancy from these previous works.

B. fcc Ni

The calculated magnetic moment for Ni in LDA is in agreement with the experiment, $0.62 \mu_B$ [32]. On the other hand, QSGW gives $0.80 \mu_B$. Sponza *et al.* [17] indicate that this is reasonable because we have not taken into account the longitudinal quantum spin fluctuation. In LDA, we may have accidentally had a good agreement because of too small exchange splitting canceling the fact that calculations do not include the fluctuation.

Figure 4(a) shows the $-\text{Im}[K^{+-}(\mathbf{q} = 0, \omega)]$ in Ni. Peaks at 0.7 eV and 0.8 eV in LDA and QSGW are the Stoner gaps, corresponding to the difference of peaks between majority and minority spins in DOS shown in the inset. ΔE_x given in LDA and QSGW are about two times larger than 0.3 eV, which is the value obtained by ARPES at the L_3 point [39]. Sponza *et al.* [17] indicate that the overestimation is due to the missing of spin fluctuations. Figures 4(b) and 4(c) show $-\text{Im}[K^{+-}(\mathbf{q}, \omega)]$ in LDA and QSGW. Our LDA results give good agreement with Fig. 6 of Ref. [35]. We see that strong intensity around Γ gets broadened as a function of \mathbf{q} as in the case of the homogeneous electron gas shown in Fig. 5 of Ref. [35]. In QSGW, the \mathbf{q} dependence of $-\text{Im}[K^{+-}(\mathbf{q}, \omega)]$ looks slightly weakened around Γ , probably because of the reflection of the flattened (weakly q -dependent) $3d$ band.

In Fig. 5(a), we show $\text{Im}[R^{+-}(\mathbf{q}, \omega)]$ in LDA. We can identify the SW dispersion in the whole Brillouin zone (BZ) in contrast to the case of Fe in Fig. 3. Our SW dispersion in LDA is consistent with a previous LR calculation by

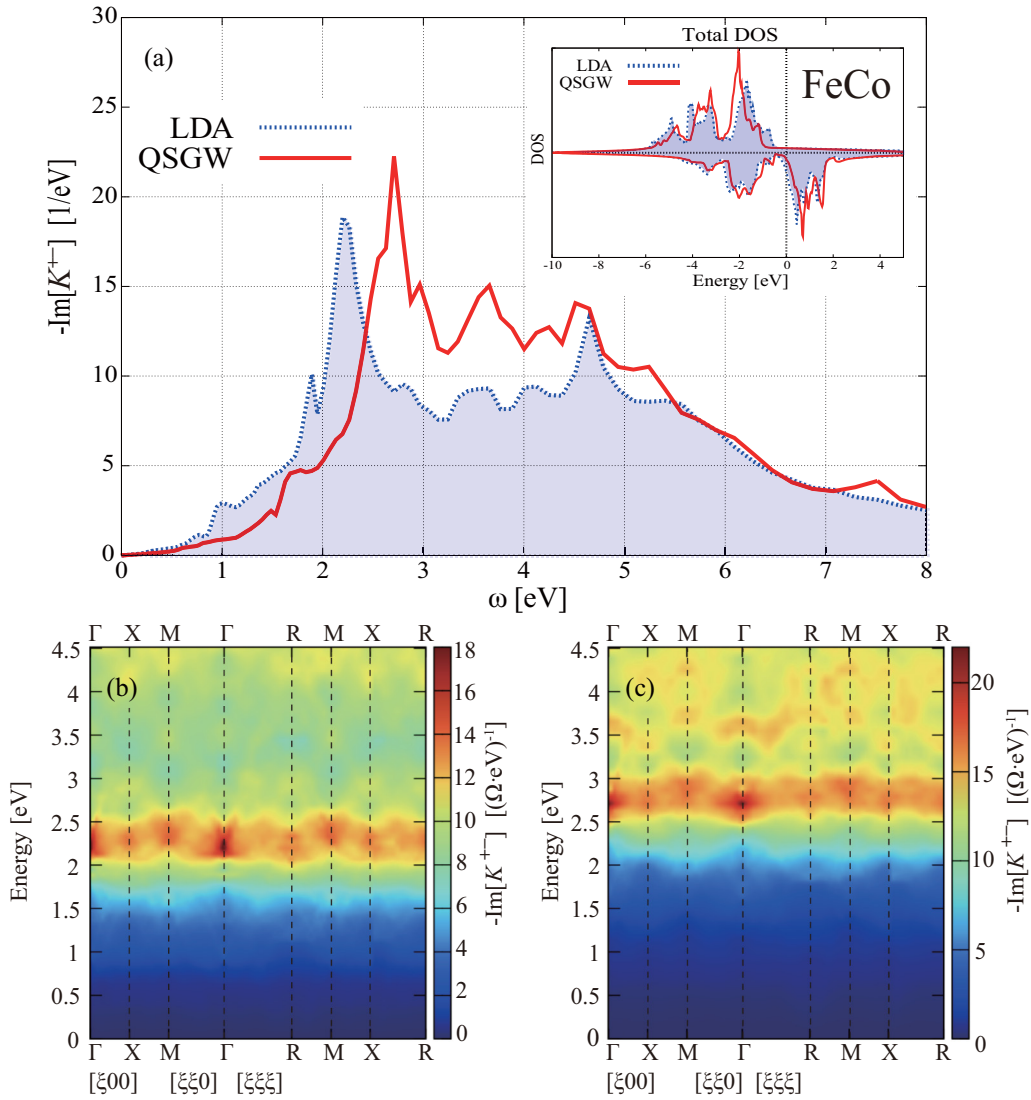


FIG. 8. (a) $-\text{Im}[K^{+-}(\mathbf{q} = 0, \omega)]$ of FeCo in QSGW (red bold line) and LDA (blue broken line). The inset is the total density of states in FeCo. Panels (b) and (c) show calculated $-\text{Im}[K^{+-}(\mathbf{q}, \omega)]$ along the BZ symmetry line in LDA and in QSGW, respectively. Ω is the unit cell volume.

Savrasov [14] and a TDDFT calculation by Niesert [37]. As superposed in Fig. 5, results with FMM [10] and with the LF [9] give a little lower $\omega(\mathbf{q})$. Let us compare the QSGW result shown in Fig. 5(b) with Fig. 5(a), where we can use black lines as a guide to the eye. $\omega(\mathbf{q})$ curvature around Γ is smaller in QSGW. In fact, Table II shows that QSGW gives very smaller $D = 449 \text{ meV } \text{\AA}^2$ around Γ than $D = 873 \text{ meV } \text{\AA}^2$ in LDA. This is in agreement with the experimental values $D = 433, 555 \text{ meV } \text{\AA}^2$ [2,40]. This is the reflection of weak \mathbf{q} dependence of $-\text{Im}[K^{+-}(\mathbf{q}, \omega)]$ around Γ in the previous paragraph. Along Γ -L, QSGW successfully traces an experiment [41] even up to half of the BZ boundary. Although (b) may be taken as a simple elongation of (a) at a glance, it is not true if we take the behavior around Γ into account. In Ref. [15], Karlsson and Aryasetiawan give good agreement with the SW dispersion along [100] by adjusting the ΔE_x of Ni. However, such a procedure may give a simple shrinkage. Thus the physical mechanism in QSGW is very different from their method

even though both our QSGW and their method reproduce the experimental D .

C. hcp Co

Figure 6(a) shows the $-\text{Im}[K^{+-}(\mathbf{q} = 0, \omega)]$ in Co and Figs. 6(b) and 6(c) show $-\text{Im}[K^{+-}(\mathbf{q}, \omega)]$ in LDA and QSGW. The calculated magnetic moment per Co atom is $1.67 \mu_B$ in LDA, $1.76 \mu_B$ in QSGW. These are a little larger than the experiment value $1.58 \mu_B$ [42]. It is reasonable in the sense that the QSGW value relative to experiment is $1.76 \mu_B / 1.58 \mu_B$, in between $2.22 \mu_B / 2.22 \mu_B$ (Fe) and $0.80 \mu_B / 0.62 \mu_B$ (Ni). Let us compare peaks of 3d shown in insets with those for Fe and Ni (Figs. 2 and 4). In QSGW, 3d bands are narrower than LDA in both the majority and minority spins in Co and Ni, in contrast to the case of Fe where there is little narrowing of DOS in the minority spins. This is probably because the bcc structure has more hybridization with sp bands than fcc and hcp. In Co, the largest peaks of 3d are pushed down by QSGW relative to LDA, with keeping

the exchange splitting. Thus changes of $-\text{Im}[K^{++}(\mathbf{q} = 0, \omega)]$ from QSGW to LDA are similar in Fe and Co. As we already noted in Sec. III A, we admit several universal tendencies of QSGW relative to LDA; however, such changes of DOS and $-\text{Im}[K^{++}(\mathbf{q} = 0, \omega)]$ are hardly predicted without calculations in practice.

In Fig. 7(a), we show $\text{Im}[R^{+-}(\mathbf{q}, \omega)]$ in LDA together with plots of the SW dispersion given by the FMM [10] (black broken lines) and by the LF [9] (black lines). In these plots, two branches appear because of two atoms per primitive cell. The LF traces peaks of our $\text{Im}[R^{+-}(\mathbf{q}, \omega)]$ very well especially along Γ -A-K-H-A. Around M, the black lines are slightly lower than the peak of $\text{Im}[R^{+-}(\mathbf{q}, \omega)]$ seen at ~ 800 meV. Near Γ , $\text{Im}[R^{+-}(\mathbf{q}, \omega)]$ shows no optical branch. Experimental data shown by oval circles [43,44] are a little lower than the plots and peaks of $\text{Im}[R^{+-}(\mathbf{q}, \omega)]$.

In contrast, we have an impressive agreement with the experiment in QSGW. As seen in Fig. 7(b), oval circles are on the peak of $\text{Im}[R^{+-}(\mathbf{q}, \omega)]$ in QSGW. The calculated D shown in Table II in QSGW are 486 meV \AA^2 along [100] and 532 meV \AA^2 along [001]. These give much better agreements with experiments, consistent with the agreement in Fig. 7(b). This agreement of the SW energy probably originates from a narrower $3d$ band in QSGW, resulting in weaker \mathbf{q} dependence of $-\text{Im}[K^{++}(\mathbf{q}, \omega)]$, rather than LDA.

D. B2 FeCo

We treat B2 FeCo in the CsCl structure. Calculated magnetic moments per cell are $4.44 \mu_B$ in LDA, $4.80 \mu_B$ in QSGW. The latter is close to experiment $4.70 \mu_B$ [45]. It is consistent with other compounds [18,19] where QSGW gives agreement with experiments as for magnetic moments when LDA gives underestimation. Alternatively, we may take FeCo as a case between Fe and Co. Since $\text{QSGW/experiment} = 2.22 \mu_B/2.22 \mu_B$ for Fe, $= 1.76 \mu_B/1.58 \mu_B$ for Co, we may say that slight overestimation $4.80 \mu_B/4.70 \mu_B$ is reasonable.

Figure 8(a) shows $-\text{Im}[K^{++}(\mathbf{q} = 0, \omega)]$ in LDA and QSGW. In its inset, ΔE_x is ~ 2.8 eV in QSGW while ~ 2.2 eV in LDA. The difference results in the difference of peaks in $-\text{Im}[K^{++}(\mathbf{q} = 0, \omega)]$. Figures 8(b) and 8(c) show $-\text{Im}[K^{++}(\mathbf{q}, \omega)]$ in LDA and QSGW, although we see no specific features worth mentioning.

Figure 9 shows $\text{Im}[R^{+-}(\mathbf{q}, \omega)]$ in (a) LDA and (b) QSGW, together with the previous SW calculation in the FMM [11]. $\text{Im}[R^{+-}(\mathbf{q}, \omega)]$ in LDA shows the lower peaks of $\omega(\mathbf{q})$ than FMM. $\text{Im}[R^{+-}(\mathbf{q}, \omega)]$ in LDA gives $D = 407 \text{ meV \AA}^2$ a little smaller than 500 meV \AA^2 by Grotheer [11]. The optical branch is weakened as in the case of Fe. The weak peak around ~ 600 meV is close to $\omega(\mathbf{q})$ in FMM.

In QSGW, there is lower $\omega(\mathbf{q})$ in the whole BZ as in the case of Co. Table II shows that $D = 307 \text{ meV \AA}^2$ in QSGW is much smaller than the experiment value $450\text{--}500 \text{ meV \AA}^2$ by inelastic neutron scattering [46]. Considering the success on Fe, Ni, and Co, this FeCo was the case for which we could expect good agreement with experiments. We have not yet found a reason why QSGW gives such discrepancy from experiment.

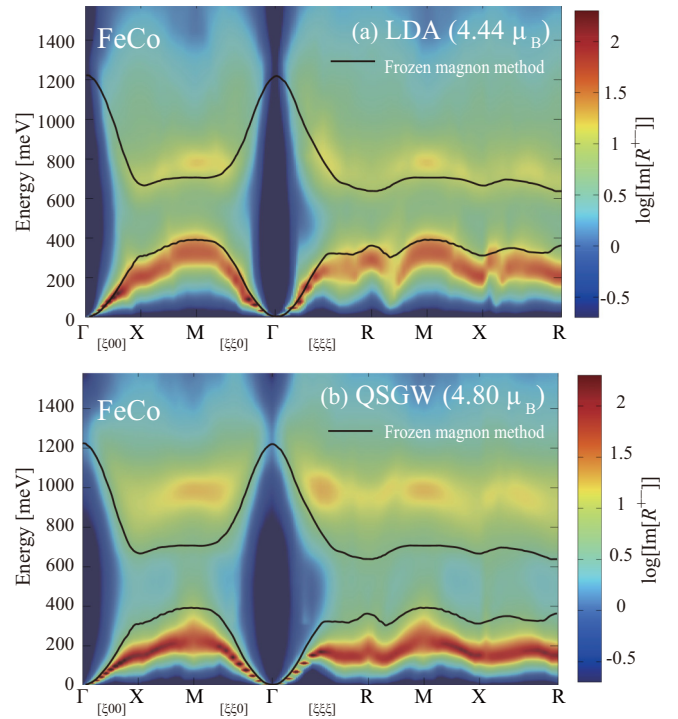


FIG. 9. $\text{Im}[R^{+-}(\mathbf{q}, \omega)]$ for FeCo (a) in LDA and (b) in QSGW, showing the SW dispersion. The black bold line shows the FMM result [11] in LDA.

IV. SUMMARY

In order to calculate SW dispersion in QSGW, we have implemented an effective numerical method for calculating $R^{+-}(\mathbf{q}, \omega)$ with the package ECALJ. This is in the linear response formulation based on the maximally localized Wannier functions as given in Ref. [16].

Then we apply the method to Fe, Ni, Co, and FeCo. We compare the peak of $\text{Im}[R^{+-}(\mathbf{q}, \omega)]$ with inelastic neutron scattering data and with the spin stiffness D . For Fe, Ni, and Co, QSGW gives much better agreements with experiment than LDA does. Notably, too large D of Ni in LDA is reduced by half, resulting in a good agreement with the experiment. We see similar agreement for Co in comparison with the neutron scattering data. For FeCo, we have not yet understood why D in QSGW disagrees with experiment.

Such good agreements are owing to the reliable description of the electronic structure in QSGW. QSGW gives a good description of $3d$ bandwidth, ΔE_x , and magnetic moments, except for the case of Ni, where we have a too large magnetic moment. Our method developed here is promising in the sense that it covers a wide range of materials from the metals treated here to transition metal oxides where LDA can be hardly applicable.

ACKNOWLEDGMENTS

This work was partly supported by the Building of Consortia for the Development of Human Resources in Science and Technology project, implemented by the Ministry of Education, Culture, Sports, Science, and Technology (MEXT) of Japan. This work was partly supported by JST CREST

Grant No. JPMJCR1812 and by JSPS KAKENHI Grant No. JP18H05212. T.K. acknowledges support by JSPS KAKENHI Grant No. 17K05499. We also acknowledge computing time

provided by the Research Institute for Information Technology (Kyushu University). We want to thank T. Fukazawa for giving us useful comments.

- [1] J. W. Lynn, *Phys. Rev. B* **11**, 2624 (1975).
- [2] H. A. Mook, R. M. Nicklow, E. D. Thompson, and M. K. Wilkinson, *J. Appl. Phys.* **40**, 1450 (1969).
- [3] F. Ye, P. Dai, J. A. Fernandez-Baca, D. T. Adroja, T. G. Perring, Y. Tomioka, and Y. Tokura, *Phys. Rev. B* **75**, 144408 (2007).
- [4] R. Vollmer, M. Etzkorn, P. S. A. Kumar, H. Ibach, and J. Kirschner, *Thin Solid Films* **464-465**, 42 (2004).
- [5] C. Kittel, *Introduction to Solid State Physics*, 8th ed. (John Wiley and Sons, 2004), p. 335.
- [6] R. Pauthenet, *J. Appl. Phys.* **53**, 8187 (1982).
- [7] A. I. Lichtenstein, M. I. Katsnelson, V. P. Antropov, and V. A. Gubanov, *J. Magn. Magn. Mater.* **67**, 65 (1987).
- [8] A. Oswald, R. Zeller, P. J. Braspenning, and P. H. Dederichs, *J. Phys. F: Met. Phys.* **15**, 193 (1985).
- [9] M. Pajda, J. Kudrnovský, I. Turek, V. Drchal, and P. Bruno, *Phys. Rev. B* **64**, 174402 (2001).
- [10] S. V. Halilov, H. Eschrig, A. Y. Perlov, and P. M. Oppeneer, *Phys. Rev. B* **58**, 293 (1998).
- [11] O. Grotheer, C. Ederer, and M. Fähnle, *Phys. Rev. B* **63**, 100401(R) (2001).
- [12] E. K. U. Gross and W. Kohn, *Phys. Rev. Lett.* **55**, 2850 (1985).
- [13] J. F. Cooke, J. W. Lynn, and H. L. Davis, *Phys. Rev. B* **21**, 4118 (1980).
- [14] S. Y. Savrasov, *Phys. Rev. Lett.* **81**, 2570 (1998).
- [15] K. Karlsson and F. Aryasetiawan, *Phys. Rev. B* **62**, 3006 (2000).
- [16] E. Şaşıoğlu, A. Schindlmayr, C. Friedrich, F. Freimuth, and S. Blügel, *Phys. Rev. B* **81**, 054434 (2010).
- [17] L. Sponza, P. Pisanti, A. Vishina, D. Pashov, C. Weber, M. van Schilfhaarde, S. Acharya, J. Vidal, and G. Kotliar, *Phys. Rev. B* **95**, 041112(R) (2017).
- [18] T. Kotani and M. van Schilfhaarde, *J. Phys.: Condens. Matter* **20**, 295214 (2008).
- [19] T. Kotani and H. Kino, *J. Phys.: Condens. Matter* **21**, 266002 (2009).
- [20] D. Deguchi, K. Sato, H. Kino, and T. Kotani, *Jpn. J. Appl. Phys.* **55**, 051201 (2016).
- [21] A first-principles electronic-structure suite based on the PMT method, the ECALJ package, is freely available at <https://github.com/tkotani/ecalj>. Its one-body part is developed based on the LMTO part in the LM Suite package. See <https://www.nnin.org/lm-suite>.
- [22] L. Hedin, *Phys. Rev.* **139**, A796 (1965).
- [23] M. S. Hybertsen and S. G. Louie, *Phys. Rev. Lett.* **55**, 1418 (1985).
- [24] M. S. Hybertsen and S. G. Louie, *Phys. Rev. B* **34**, 5390 (1986).
- [25] M. van Schilfhaarde, T. Kotani, and S. Faleev, *Phys. Rev. Lett.* **96**, 226402 (2006).
- [26] T. Kotani, *J. Phys. Soc. Jpn.* **83**, 094711 (2014).
- [27] T. Kotani, H. Kino, and H. Akai, *J. Phys. Soc. Jpn.* **84**, 034702 (2015).
- [28] C. Friedrich, E. Şaşıoğlu, M. Müller, A. Schindlmayr, and S. Blügel, Spin excitations in solids from many-body perturbation theory, *First Principles Approaches to Spectroscopic Properties of Complex Materials*, edited by C. Di Valentin, S. Botti, and M. Cococcioni, Topics in Current Chemistry (Springer, Berlin, Heidelberg, 2014), Vol. 347, pp. 259–301.
- [29] N. Marzari and D. Vanderbilt, *Phys. Rev. B* **56**, 12847 (1997).
- [30] I. Souza, N. Marzari, and D. Vanderbilt, *Phys. Rev. B* **65**, 035109 (2001).
- [31] T. Kotani and M. van Schilfhaarde, *Solid State Commun.* **121**, 461 (2002).
- [32] H. Danan, A. Herr, and A. J. P. Meyer, *J. Appl. Phys.* **39**, 669 (1968).
- [33] A. L. Kutepov, *J. Phys.: Condens. Matter* **29**, 465503 (2017).
- [34] J. Schäfer, M. Hoinkis, E. Rotenberg, P. Blaha, and R. Claessen, *Phys. Rev. B* **72**, 155115 (2005).
- [35] C. Friedrich, M. C. T. D. Müller, and S. Blügel, Spin excitations in solid from many-body perturbation theory, *Handbook of Materials Modeling*, edited by W. Andreoni and S. Yip (Springer, Cham, 2018), pp. 1–39.
- [36] C. K. Loong, J. M. Carpenter, J. W. Lynn, R. A. Robinson, and H. A. Mook, *J. Appl. Phys.* **55**, 1895 (1984).
- [37] M. Niesert, *Ab initio* calculations of spin-wave excitation spectra from time-dependent density-functional theory, Ph.D. thesis, RWTH Aachen University, 2011.
- [38] See Supplemental Material at <http://link.aps.org/supplemental/10.1103/PhysRevB.100.054419> for detailed fitting results of SW dispersion.
- [39] D. E. Eastman, F. J. Himpsel, and J. A. Knapp, *Phys. Rev. Lett.* **44**, 95 (1980).
- [40] H. A. Mook, J. W. Lynn, and R. M. Nicklow, *Phys. Rev. Lett.* **30**, 556 (1973).
- [41] H. A. Mook and D. M. Paul, *Phys. Rev. Lett.* **54**, 227 (1985).
- [42] H. P. Myers and W. Sucksmith, *Proc. R. Soc. London A* **207**, 427 (1951).
- [43] T. G. Perring, A. D. Taylor, and G. L. Squires, *Phys. B (Amsterdam)* **213-214**, 348 (1995).
- [44] G. Shirane, V. J. Minkiewicz, and R. Nathans, *J. Appl. Phys.* **39**, 383 (1968).
- [45] J. E. Goldman and R. Smoluchowski, *Phys. Rev.* **75**, 310 (1949).
- [46] R. D. Lowde, M. Shimizu, M. W. Stringfellow, and B. H. Torrie, *Phys. Rev. Lett.* **14**, 698 (1965).